

Nanoceria-Based Phospholipase-Mimetic Cell Membrane Disruptive Antibiofilm Agents

Kritika Khulbe, Kapudeep Karmakar, Sourav Ghosh, Kasturi Chandra, Dipshikha Chakravorty,* and Govindasamy Mughesh*

Cite This: <https://dx.doi.org/10.1021/acsabm.0c00363>

Read Online

ACCESS |

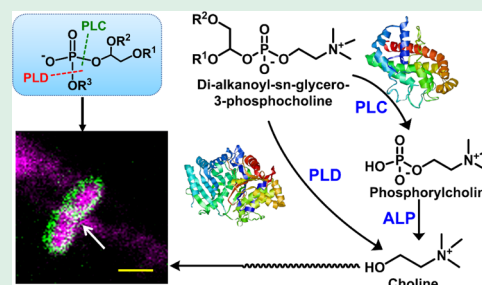
Metrics & More

Article Recommendations

Supporting Information

ABSTRACT: Continuous mounting of antibiotic resistance due to the narrow range of mechanisms targeted poses tremendous threat to global health. Highly resistant pathogenic bacteria dwelling in the biofilm mode on the surface of medical devices has increased the susceptibility of chronic as well as healthcare-associated infections. Lantipeptides have shown promising membrane disruption of Gram-positive bacteria, leading to programmed cell death, but they are impermeable and hence ineffective to the outer cell membrane of Gram-negative bacteria. Herein, we report for the first time that a polymer-coated nanoceria (PAA-Cnp) having phospholipase-mimetic activity can target the cell membrane of both Gram-negative and Gram-positive bacteria. The nanozyme shows promising membrane disruption-based bactericidal activity against a broad spectrum of pathogenic as well as biofilm-encased bacteria. The unprecedented nanozyme-based strategy described in this paper is useful in preventing biofilm formation on medical devices such as urinary catheters.

KEYWORDS: antibiotic, biofilm, nanozyme, phospholipase, urinary tract infection



1. INTRODUCTION

With the Nobel Prize winning discovery of penicillin by Sir Alexander Fleming, Ernst Boris Chain, and Sir Howard Walter Florey, an early warning was delivered by the scientists regarding antimicrobial resistance (AMR), and soon, the initial phase of chemotherapeutic effects of antimicrobial drugs was abrogated by their increased exposure.^{1,2} Continuous increase in the breadth of resistant antibiotics and microbes due to the lack of antimicrobial therapeutics has resulted in the United Nations General Assembly declaration of AMR as the fourth important health issue in 2016.³ The existing antibiotics mainly target genotypic features such as cell wall, DNA, protein expression of specific pathogenic bacteria, or more recently phenotype-based biochemical assays, enzyme inhibitors, and so forth, which are mostly centered around known biosynthetic pathways.^{4–7} Among the new approaches, various types of nanomaterials exhibited promising antibacterial properties mainly because of (a) their stability preventing degradation by bacterial enzymes, (b) permeability through the outer cell membrane, and (c) poor efflux rates as compared with small-molecule substrates.⁸ A few reports on metal and metal-oxide-based hybrid nanostructures (Au, TiO₂, Fe₃O₄, ZnO/Au, Ag, etc.) as well as artificial enzymes (graphene quantum dots, V₂O₅, CeO₂, etc.) with different forms of bactericidal effects have been explored.^{8–20} However, the narrow range of mechanisms targeted by the limited class of antibacterial compounds was not helpful in prolonging the bacteria to acquire new ways of resistance.^{6,21}

Medical devices such as catheters, syringes, contact lenses, and orthopedic implants provide surfaces for sessile bacteria to adhere and develop matrix-enclosed structures comprising mainly exopolysaccharides (EPS), called biofilms.^{22–24} Biofilms provide an effective shelter for the bacteria against environmental conditions such as osmotic and antibiotic stress, resulting in 100–1000-times higher resistance and reduced susceptibility toward host–immune defenses, leading to chronic health infections.^{25–32} As a consequence, medical devices contribute to major healthcare-associated infections and expose patients to high risk of device replacement. There is an urgent need to develop new strategies by finding out new cellular targets and molecular mechanisms to curb the increasing population of AMR organisms.

The generation of short-lived radical species, such as •OH and •O₂, for eradication of bacteria and disruption of biofilms has been explored earlier through cerium oxide and several other metal or metal-oxide-based nanomaterials.^{8,9,14,15,33–38} However, targeting biofilms at the air–liquid interface such as pellicle-like, floating biofilms formed by *Escherichia coli* and *Salmonella enterica* is a challenging task as

Received: April 3, 2020

Accepted: May 22, 2020

Published: May 22, 2020

the radical species cannot diffuse to the surface.^{39,40} The versatile multi-enzyme-mimetic properties of CeO₂-based nanomaterials have gained attention as a phosphor-ester hydrolytic agent.^{41–45} The presence of mixed oxidation state active site of Ce³⁺ and Ce⁴⁺ ions is mainly responsible for a base-mediated nucleophilic attack of the organophosphate P center, facilitating the hydrolysis reaction.^{15,43–45} In 2016, Qu et al. reported a ceria complex-based DNase-mimetic nanozymes which show potent biofilm disruption activity on *Staphylococcus aureus*.¹⁵

In this paper, we utilized the hydrolytic activity of nanoceria to target the cell membrane of the bacteria. We describe for the first time the design and cell membrane degradation ability of a remarkable phospholipase-like active ceria nanozyme. In our polymer-conjugated ceria nanozyme architecture, the dual oxidation state (Ce³⁺ and Ce⁴⁺) surface provided catalytic site for binding and hydrolysis of long-chain phospholipids present on the bacterial cell membrane, whereas the polymer coating provided sufficient dispersibility to the nanostructure for enhanced antibacterial activity. Interestingly, the novel phospholipase-like activity of polyacrylic acid (PAA) coating on the surface of ceria nanozyme favors spatiotemporal interaction with the lipophilic cell membrane showing global bactericidal effect on a broad spectrum of human pathogens such as gastrointestinal pathogens (*E. coli*, *Salmonella* Typhi, *Vibrio cholerae*, and *Shigella flexneri*) and respiratory pathogens (*Klebsiella pneumoniae*) associated with various chronic infections. Unlike conventional antibiotics, nanozymes could permeate and attack the biofilm-encased cells, an activity which is unique to nanomaterials. This novel phospholipase-like activity of nanoceria was further employed in coating the inner surface of urinary catheters showing promising antibiofilm effect.

2. RESULTS AND DISCUSSION

2.1. Synthesis and Characterization of Nanoparticles.

CeO₂ (Cnp) was synthesized by a hydrothermal method under mildly reducing conditions as reported earlier.⁴⁷ In order to prepare PAA-coated CeO₂ (PAA-Cnp) nanoparticles, a base-mediated coprecipitation method was used, and the coated nanoparticles were isolated via a membrane filter.⁴⁶ The scanning electron microscopy (SEM) images of the nanomaterials showed agglomerated particles, which upon sonication in acetone revealed a particle-like morphology (size ~10 nm) in the transmission electron microscopy (TEM) images (Figures 1a and S1a–f). Powder X-ray diffraction patterns showed a cubic fluorite lattice for both the nanomaterials (JCPDS no. 01-0800 for CeO₂) (Figure S2). Energy-dispersive spectroscopy and X-ray mapping analysis confirmed the elemental purity of the nanoparticles (Figure S3a–c).

An overall negative charge imparted on the surface of PAA-Cnp (-38.7 ± 2.56 mV) compared to the positively charged Cnp (25.1 ± 0.45 mV) confirmed that PAA was coated on nanoceria (Figure 1b). Further, confirmation of PAA coating on nanoceria was obtained by Raman spectroscopic analysis of PAA-Cnp. While the Raman spectra of Cnp and PAA-Cnp showed a characteristic peak for Ce–O stretching around 460 cm⁻¹, the additional peaks observed for PAA-Cnp at 1048 and 2931 cm⁻¹ corresponding to –CH₂– and –CH– stretching, respectively, confirmed that PAA was coated on the nanoceria surface (Figure 1c).⁴⁸ The absence of –CO₂H– stretching in the Raman spectra of PAA-Cnp indicates that the –CO₂H– group in PAA is responsible for anchoring on nanoceria surface

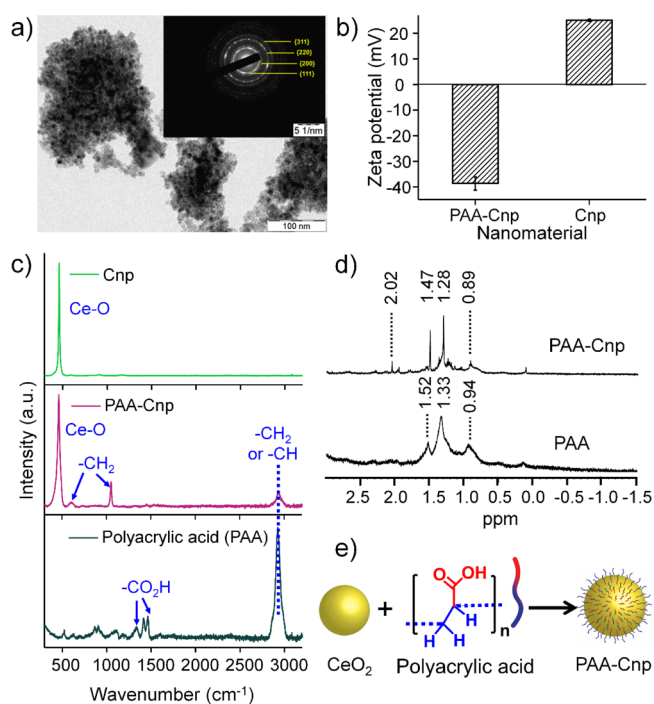


Figure 1. (a) TEM image and selected area electron diffraction pattern (inset) of PAA-Cnp. (b) Zeta potential of nanoceria (Cnp) and PAA-coated nanoceria (PAA-Cnp) showing surface charge in the positive potential and negative potential region, respectively. (c) FT-Raman spectra of PAA, PAA-Cnp, and Cnp. The peaks corresponding to –CH₂ and –CH were observed both in PAA and in PAA-Cnp. The characteristic peak for the Ce–O vibration (460 cm⁻¹) was observed in PAA-Cnp matched with nanoceria (Cnp). The absence of carboxylic (–CO₂H) stretching vibration (1450 cm⁻¹) in PAA-Cnp confirmed that the carboxylic moiety of PAA attached primarily with the CeO₂ surface. (d) ¹H NMR spectra of PAA-Cnp and PAA (top to bottom) showing peaks for aliphatic carbons in the polymer backbone of PAA and PAA-Cnp. The peak observed at 2.02 ppm in the PAA-Cnp NMR spectrum is due to the fragmented PAA. (e) Schematic representation of PAA-coated CeO₂ nanoparticles (PAA-Cnp).

(Figure 1c). A similar observation was obtained from the Fourier transform infrared (FT-IR) spectra of PAA-Cnp (Figure S4).⁴⁸ Attachment of PAA to nanoceria was further confirmed by recording the ¹H NMR spectra of PAA-Cnp. Three major peaks observed in the range of 0.8–1.5 ppm in the ¹H NMR spectra of PAA-Cnp correspond to the aliphatic protons in the PAA backbone (Figure 1d). An additional peak at 2.0 ppm for the terminal –CH₃ was detectable only in the PAA-Cnp spectra, indicating that the long polymeric chain is broken into smaller fragments while wrapping around nanoceria by means of weak interactions (Figure 1d).⁴⁹ Based on these results, the basic structural model of PAA-Cnp was designed (Figure 1e).

2.2. Study of in Vitro Phospholipase Activity.

Phospholipase activity can be categorized into four types based on the site of cleavage of the phospholipid (substrate), namely, phospholipase A₁ (PLA₁), A₂ (PLA₂), C (PLC), and D (PLD) (Figure S5a). First, we analyzed the phospholipid hydrolytic activity of ceria-based nanoparticles by matrix-assisted laser desorption ionization (MALDI)-mass analysis using glycerophosphate substrate, 1-palmitoyl-2-oleoyl-*sn*-glycero-3-phosphoglycerol (POPG). The MALDI spectra was recorded after the reaction of POPG with either PAA-Cnp or Cnp (100 μg/mL used for both nanocatalysts) and showed a

new peak at 577 m/z , which was assigned for 3-(palmitoyloxy)prop-1-en-2-yl oleate ($M + H^+$) (Figures 2a

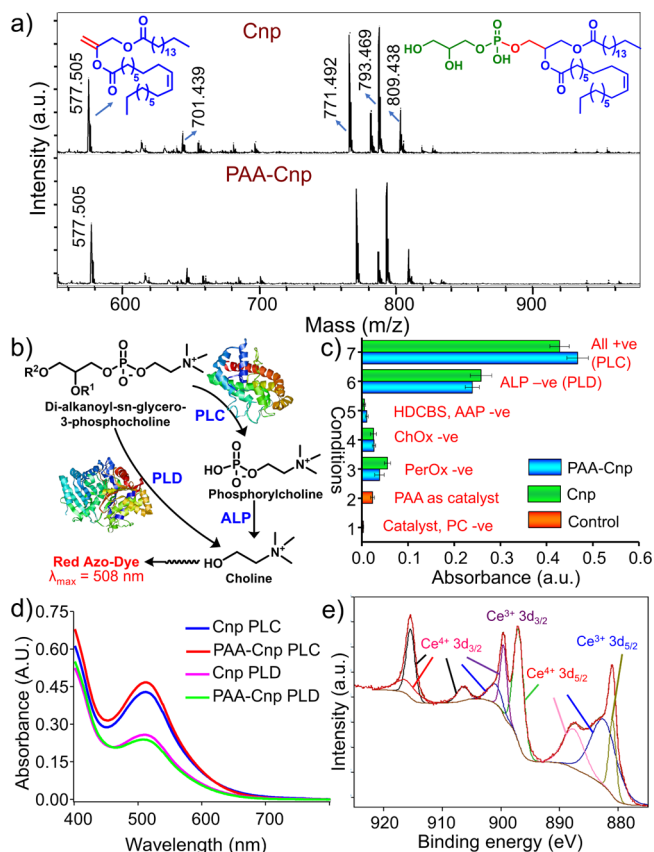


Figure 2. (a) MALDI-mass obtained after the hydrolysis of substrate (POPG) treated with Cnp or PAA-Cnp in Tris buffer pH 7.8 at 37 °C for 36 h. The peaks for POPG appeared at 771.5 ($M + Na^+$), 793.5 ($M + 2Na^+$), and 809.4 ($M + Na^+ + K^+$) m/z , whereas the peaks at 577 and 701.44 m/z were due to the products formed by the PLC and PLD pathways, respectively. (b) Schematic representation of the UV-vis assay for monitoring the PLC and PLD activity of enzyme using a phosphatidylcholine (PC) substrate. In both the cases, the final product is the formation of a red chromogen azo-dye (λ_{max} at 508 nm). Unlike PLD, alkaline phosphatase (ALP) enzyme is involved with the reaction scheme of PLC to form the azo-dye (detailed scheme shown in Figure S6). (c) Bar diagram quantification of the intensity of red azo-dye and (d) UV-vis spectra showing plot for absorbance vs wavelength for the hydrolysis of PC by Cnp or PAA-Cnp in Tris buffer pH 7.8 at 37 °C for 36 h, followed by incubation of the isolated product with the enzyme and dye mixture (all components for the PLC assay: catalyst + PC + PerOx + ChOx + ALP + HDCBS + AAP). (e) XPS analysis of Ce 3d deconvoluted spectra for Cnp depicting Ce in both +3 and +4 oxidation states.

and S5b), indicating that the hydrolysis of POPG by ceria-based catalysts proceeded with the cleavage of the long alkoxy tail. However, a small peak at 701.44 m/z was assigned for 1-palmitoyl-2-oleoyl-*sn*-glycero-3-phosphate ($M + 3H^+ + Na^+$) product owing to the removal of polar glycerol moiety from POPG (Figure 2a). This confirmed that the ceria-based nanocatalysts were capable of hydrolyzing phospholipids such as POPG mainly by a phospholipase C (PLC)-mediated pathway and minimally by a phospholipase D (PLD)-like activity. The complete absence of peaks for palmitic acid or oleic acid products around 500 and 460 m/z , respectively,

confirmed that neither PLA₁ nor PLA₂ esterase-like activity was shown by either of the nanoparticles (Cnp and PAA-Cnp).

Further, to ascertain the probability of PLC versus PLD activity on the surface of nanoceria, the UV-vis spectroscopy-sensitive dye-based assay was carried out. In this previously reported assay, PC (phosphatidyl choline; lecithin), a major component of the biological membrane, upon hydrolysis by a PLC-mediated pathway gives phosphoryl choline as a product, whereas via the PLD-mediated pathway, choline is formed (Figure 2b). Hence, ALP enzyme is involved in the PLC-mediated pathway to form choline from PC, which is converted finally to the red chromogen azo-dye (absorption λ_{max} @ 508 nm) (Figure S6).⁵⁰

From the bar diagram shown in Figure 2c, it is clear that when any of the assay components (except for ALP) is absent from the reaction mixture, a negligible intensity of the dye at λ_{max} 508 nm was observed, indicating that both the ceria-based nanomaterials show true phospholipase C and D mimetic activity. A greater absorbance intensity was observed for the red azo-dye ($\lambda_{max} = 508$ nm) when all the reaction components (including ALP) were present in the reaction mixture, indicating that both the nanozymes show mainly PLC-like activity (bar diagram shown in Figure 2c). However, the intensity of red-azo dye formed by hydrolysis of PC by Cnp and PAA-Cnp commensurates with each other, showing that PAA coating does not alter the overall reactivity of nanoceria (Figure 2c,d). Also, when PAA was used for the reaction, no azo-dye was formed, indicating that PAA has no role in the hydrolysis of PC (Figure 2c).

It is well known that surface properties play a major role during catalysis on the nanozyme surface. Analysis of the facets exposed on the surface of nanozymes by high-resolution TEM images and the corresponding fast Fourier transform patterns showed that in the cubic-fluorite lattice of Cnp and PAA-Cnp, the atomic arrangement of planes was aligned along the $[0 -1 1]$ zone axis and mainly exposed the $\{110\}$ facets (Figure S11b,c). We estimated the oxygen vacancies in Cnp and PAA-Cnp nanozymes using X-ray photoelectron spectroscopy (XPS).^{51–53} The presence of mixed Ce^{3+} and Ce^{4+} oxidation states in the deconvoluted Ce 3d XPS spectra confirmed the presence of oxygen vacancies on the surface of both the nanozymes (Figures 2e and S11a) coherent with the fact previously reported that the reactivity of vacancy generation among different ceria facets follow the order: $\{110\} > \{100\} > \{111\}$.^{54–56} This indicates that PAA coating on nanoceria does not alter its surface properties. The phospholipase activity shown by the nanoparticles is the intrinsic property of the nanoceria surface containing dual oxidation state (Ce^{3+} and Ce^{4+}) active site pocket (Scheme S1). Based on the previous reports of phosphohydrolase activity of vacancy-engineered nanoceria,⁴³ we anticipated that PC (harder base) would bind with the Ce^{4+} ion at the catalyst pocket, whereas base generation from water (softer base) would occur at the Ce^{3+} site. Hence, we proposed the model for base-mediated hydrolysis of phospholipid diester on the surface of nanoceria as shown in Scheme S1.

2.3. Study of Kinetic Parameter for Phospholipase C Activity of Ceria-Based Nanocatalysts. As the nanocatalysts mainly exhibited PLC-like activity, the catalytic parameters were found using model substrate, *p*-nitrophenyl phosphoryl choline (NPPC) (Figure S7a,b).^{57,58} The hydrolysis of NPPC using Cnp and PAA-Cnp (100 $\mu g/mL$ used for both nanocatalysts) was monitored by the UV-vis absorption

spectra of the final product *p*-nitrophenol, which showed absorption maxima at 405 nm.

It was observed that, initially, the rate of conversion of NPPC to *p*-nitrophenol by Cnp was much greater than PAA-Cnp; however, a proportionate amount was formed by both nanocatalysts at later time points (Figures 3a and S7c),

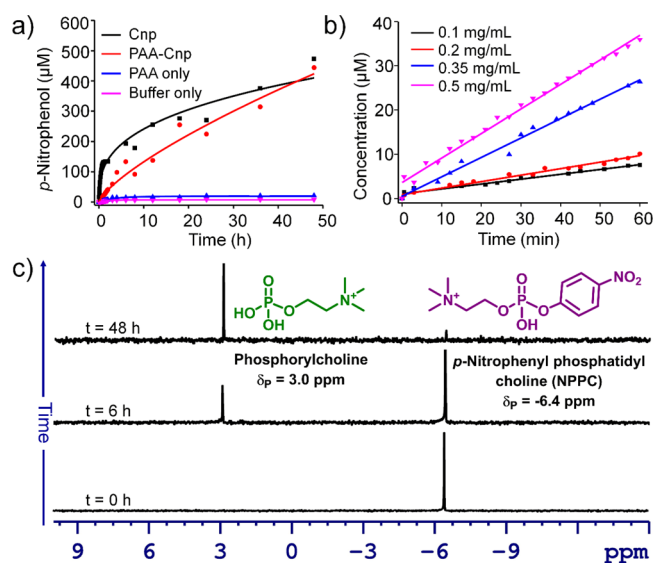


Figure 3. (a) Time-dependent analysis of increase in *p*-nitrophenol formation by hydrolysis of NPPC using nanozyme, Cnp, and PAA-Cnp in the presence of Tris buffer pH 7.8 at 37 °C by monitoring the increase in the absorbance intensity of peak at 405 nm. (b) Plot of *p*-nitrophenol ($\lambda_{\max} = 405$ nm) as a function of time formed after the hydrolysis of NPPC (4.0 mM) by different concentrations of PAA-Cnp in Tris buffer pH 7.8 at 37 °C monitored by UV–vis spectroscopy. (c) ³¹P NMR spectroscopy analysis for the hydrolysis of NPPC (1.0 mM) by Cnp, showing formation of phosphorylcholine in Tris buffer pH 7.8 at 37 °C at different time points.

probably because of the saturation of the active site of Cnp. Further, the variation of initial rate of decomposition of different concentrations of NPPC followed a sigmoidal curve, indicating that the nanocatalyst shows Michaelis–Menten enzyme kinetics (Figure S8). From the catalytic parameters, we found that the K_M of PAA-Cnp \gg Cnp, which implies that the substrate binding affinity of Cnp is greater than that of PAA-Cnp, leading to more probability of active site saturation in the case of Cnp (Table S1). Indeed, the V_{\max} values for NPPC hydrolysis by PAA-Cnp and Cnp were observed to be comparable again, correlating with the previous conclusion (Table S1). Increasing the concentration of PAA-Cnp increased the rate of the reaction, indicating that the reaction, indeed, occurs at the active site of the catalyst surface (Figures 3b and S7d).

Elucidation of the product formed from the hydrolysis of NPPC by the nanozymes was done by ³¹P NMR spectroscopic studies. It was observed that, upon reaction with the nanozymes, Cnp and PAA-Cnp, the peak for the starting material (NPPC) at -6.4 ppm disappeared, and a new peak for phosphorylcholine emerged at 3.0 ppm, indicating that NPPC undergoes a one-step hydrolysis (Figures 3c and S9) unlike the control experiment, where no hydrolysis occurred (Figure S10). This confirmed that the nanozyme carried out a single-step hydrolysis of the phospholipid substrate.

2.4. Effect of Phospholipase-Mimetic Activity of Ceria-Based Nanozymes on the Cell Membrane of Bacteria.

Phospholipids form the major component of bacterial cell membrane; therefore, we extended the study of phospholipase-mimetic activity of ceria-based nanozymes, Cnp and PAA-Cnp (50 μg/mL used for both nanocatalysts) in vivo. First, we monitored the alteration in the bacterial membrane potential upon treatment of our nanozymes using an anionic dye, bis-(1,3-dibutylbarbituric acid)trimethineoxonol (Di-BAC₄(3)). The depolarization of the bacterial cell membrane due to PAA-Cnp and Cnp administration for 24 h was evident from the pale blue coloration of the cells stained with the dye similar to the positive controls, CTAB and ampicillin, unlike the deep blue colored cells in the untreated case. This proved that treatment of cells with nanozymes leads to disintegration of the cell membrane, probably because of the hydrolysis of phospholipids (Figures 4a and S12a). Based on the decoloration of dye, the cells treated with PAA-Cnp were assumed to be more depolarized compared to Cnp-treated cells. At later time points (48 h), the SEM images of bacterial cells treated with and without PAA-Cnp were taken. Although the field of untreated cells showed densely populated bacterial cell colonies, the PAA-Cnp treated cells formed sparse colonies with cytoplasmic leakage from the ruptured cells, characterizing bacterial cell membrane damage (Figure 4b,c).

Further, the cell membrane damage was indicated using a dye specific for staining the cell membrane phospholipids, *N*-(3-triethylammoniumpropyl)-4-(6-(4-(diethylamino)phenyl)hexatrienyl)pyridiniumdibromide (FM4-64).^{59,60} It was observed that the cell membrane of *Salmonella* bacteria grown in LB (luria broth) in the presence of Cnp and PAA-Cnp was completely ruptured, resulting in leakage of DNA (labeled by DAPI) from the damaged cells unlike the well-confined cellular matrix of the untreated cells (Figure 4d–f). Because LB is a nutrient-rich media, we used M9 minimal media (supplemented with 0.05% glucose as the carbon source) to observe the effect of Cnp or PAA-Cnp treatment on the cell membrane and found that this phospholipase-like activity-mediated membrane degradation is independent of the media used (Figure S12b). However, no DNA leakage was observed under log-phase condition in either of the media, indicating that the nanozymes show inactivity during this rapid cell division phase where repair of damaged cell membrane is possible (Figure S13). However, during the stationary phase, when the synthesis of cell membrane is halted because of nutrient depletion, the in vivo phospholipase-mimetic activity of PAA-Cnp and Cnp nanozymes showed effective cell membrane degradation.⁶¹

2.5. Stationary-Phase Antibacterial Effect and Inhibition of Biofilm Formation by Phospholipase-Mimetic Ceria-Based Nanozyme.

A comparison of the antibacterial effect of Cnp and PAA-Cnp nanozymes (50 μg/mL used for both nanocatalysts) on *Salmonella* culture at the stationary phase through quantification of the colony-forming units (cfu) showed more than 1.5 and 1 log fold reduction in the bacterial cell count, respectively, compared to the untreated bacteria in both LB and M9 minimal media (Figures 5a and S14). The dead bacterial population was also visualized using a confocal microscope after staining with propidium iodide (PI), which is impermeable to live cells. The number of PI-positive cells was higher under PAA-Cnp-treated condition specifically in the stationary phase (Figure 5b) but not in log phase (Figure S15). A quantification of the dead bacteria after nanozyme treatment

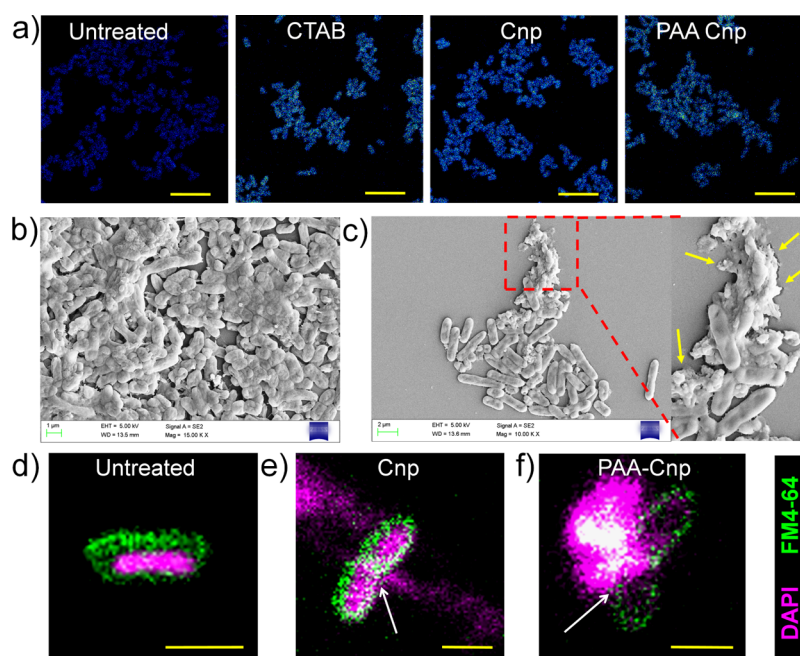


Figure 4. (a) Confocal images show depolarization of bacterial cell membrane after treatment with PAA-Cnp using DiBAC₄ (3) staining. CTAB-treated cells were used as a positive control for depolarization in comparison with untreated cells. Scale bar = 2 μ m. (b,c) SEM images of *Salmonella* bacteria after 48 h growth in media only and in media containing PAA-Cnp, respectively, showing cytoplasm leakage and damaged cells (marked in yellow arrows) in the latter case. (d–f) Confocal microscopy images of damaged bacterial cell membranes of *Salmonella* bacteria grown in LB media by Cnp and PAA-Cnp. Membrane damage was visualized using FM4-64 dye (for staining a lipid bilayer), and DNA leakage from cells (white arrows) was visualized by 4',6-diamidino-2-phenylindole (DAPI).

shows about 80% biocidal activity of PAA-Cnp on *Salmonella* (Figure S34). However, when the stationary-phase bacteria were treated with PAA alone, no PI-positive cells were observed similar to the untreated case (Figure S16). The minimum inhibitory concentration (MIC) of our nanozymes (≥ 100 μ g/mL) was found to be higher as compared with the well-known antibacterial Ag nanoparticles, confirming again that they have lower susceptibility toward the log-phase *Salmonella* bacterium (Figure S33a). A similar result was observed for another type of Gram-negative bacteria, *E. coli* (Figure S33b). However, for the biocompatibility study, HeLa cells were incubated with the nanoparticles and checked for cell viability using the MTT assay, suggesting that the Ag nanoparticles have an indiscriminatory toxic effect toward both bacterial and mammalian cells, whereas the ceria-based nanozymes, PAA-Cnp and Cnp, showed no toxicity toward the mammalian cells at early (12 h) or late time points (72 h) (Figure S35a,b). The cells incubated with 25 μ g/mL of Ag nanoparticles and 50 μ g/mL of Cnp showed lesser viability, whereas PAA-Cnp and 25 μ g/mL of Cnp did not cause any significant cytotoxicity.

Next, we studied the antibacterial effect of our nanozymes on the two distinct stages of biofilm formation: the first step involving the initial attachment of bacteria to the substratum and the second step is the process of EPS secretion and pellicle formation. It was observed that during the initial attachment stage, when the bacteria adhered to the coverslip, the treatment with PAA-Cnp leads to bacterial killing (Figure S17). However, for the nanoparticles to show antibacterial activity during the second stage of biofilm formation, the particles should penetrate the EPS matrix. One of the main reasons for inactivity of antibiotics and development of antimicrobial

resistance is the inability to penetrate inside the biofilm acting as a protective shield against the antibiotics.^{21,23,29}

Using FITC-tagged PAA-Cnp (synthesis and characterization shown in Figures S18–S20), we tested the biofilm penetrating ability of our antibacterial nanozyme. The presence of green fluorescent FITC-tagged PAA-Cnp nanozyme was observed in blue fluorescent DAPI-stained biofilms grown till 5 days, 7 days, and 10 days (Figures 5c,d and S21), showing the permeability of the nanometric-sized particles through thick biofilms. The cells harvested from these biofilms were found positive for PI, indicating that PAA-Cnp retains the antibacterial activity inside the preformed biofilm as well (Figure 5e). Further validation about the cell viability was done using the cfu counts of the preformed biofilms. It was observed that the PAA-Cnp-treated biofilms showed significantly reduced bacterial cfu (>1 -log fold) as compared to the untreated cells (Figure 5f).

As it is known that nutrient-depleted conditions trigger the formation of biofilms, we compared the biofilm inhibition property of PAA-Cnp and Cnp with known antibiofouling and antibacterial agents. *Salmonella* was chosen as a model bacterium because of its ability to form a visible biofilm even without staining.⁶² The antibiofilm activity was monitored on the stationary-phase cultures of *Salmonella* coincubated with the nanomaterials based on the crystal violet (CV) staining assay. Interestingly, the phospholipase-mimetic PAA-Cnp, at a concentration ≥ 5 -fold lower than the MIC value (50 μ g/mL), showed greater intensity of biofilm inhibition compared to known antibiofouling agents, such as haloperoxidase-mimetic V₂O₅ and CeO₂, even in the absence of H₂O₂ and KBr (Figure 6a). It should be noted that although PAA-Cnp showed slower phospholipase activity than Cnp *in vitro*, the enhanced *in vivo* activity was attributable to the presence of polymer coating,

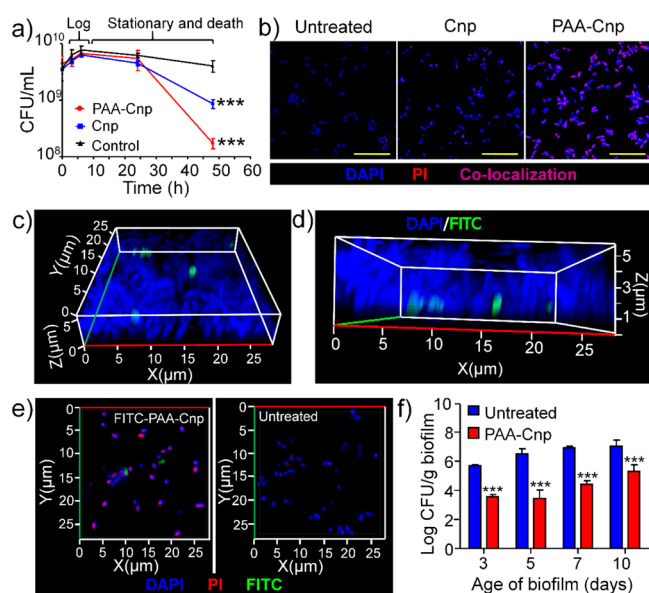


Figure 5. (a) Time-dependent cfu analysis of the growth of *Salmonella* in M9 minimal media upon pretreatment with 50 $\mu\text{g}/\text{mL}$ of Cnp and PAA-Cnp. Both the nanoparticles showed antibacterial activity exclusively in the stationary phase as compared to the control. PAA-Cnp showed >1-log fold reduction in cfu than in control. One-way ANOVA with Bonferroni post-test was used to analyze the results. $P < 0.001 = ***$. (b) Confocal microscopy images show live and dead cells of *Salmonella* bacteria treated with 50 $\mu\text{g}/\text{mL}$ of Cnp and PAA-Cnp. DAPI (blue) and PI dyes (red) were used to stain bacteria and dead cells, respectively. (Scale bar = 5 μm). (c,d) Representative 3D confocal images of the preformed *Salmonella* biofilm grown till 7 days of post-treatment with fluorescein isothiocyanate (FITC)-tagged PAA-Cnp. (e) Confocal microscopy images show the viability of bacterial cells after treatment with FITC-tagged PAA-Cnp on the preformed biofilm. (f) Bar diagram shows the quantification of cfu of *Salmonella* harvested from the biofilm of different ages treated with or without PAA-Cnp. One-way ANOVA was used to analyze the result. $P < 0.001 = ***$ and $P < 0.01 = **$.

which imparts greater dispersibility to the nanoceria.⁶³ It was found that upon leaving the sonicated nanoparticles undisturbed for 6 days, PAA-Cnp remained dispersed in the solution, whereas Cnp was mostly settled at the bottom (Figure S22). Next, we checked the antibiofilm activity by coating nanoceria with other ligands, such as citrate and dextran, which are known to show antibacterial activity.^{33,38} Indistinguishably, the antibiofilm activity of PAA-Cnp was found to be greater than other known antibacterial agents for *Salmonella* biofilms based on the CV staining assay (Figure 6b). However, the antibiofilm property was also exhibited by bare Cnp but to a lesser extent and was never exhibited by its bulk form (Figure 6c). Weakening of the biofilm architecture formed upon the growth of *Salmonella* with PAA-Cnp was found comparable to the negative control (*Salmonella* mutant ΔcsgD strain), which lacks the transcription factor responsible for regulating biofilm formation (Figure 6d). This again confirmed that phospholipase-mimetic PAA-Cnp was capable of biofilm disruption. Further, visualization of the biofilm structure through SEM showed that under PAA-Cnp-treated condition, sparse biofilms were found attached to the cover slips (Figure S23). The formation of a biofilm by PAA-Cnp was also compared with highly efficient oxidase-mimetic nanozyme, MnFe_2O_4 .⁶⁴ It was found that MnFe_2O_4 showed negligible biofilm inhibition compared to PAA-Cnp (Figure

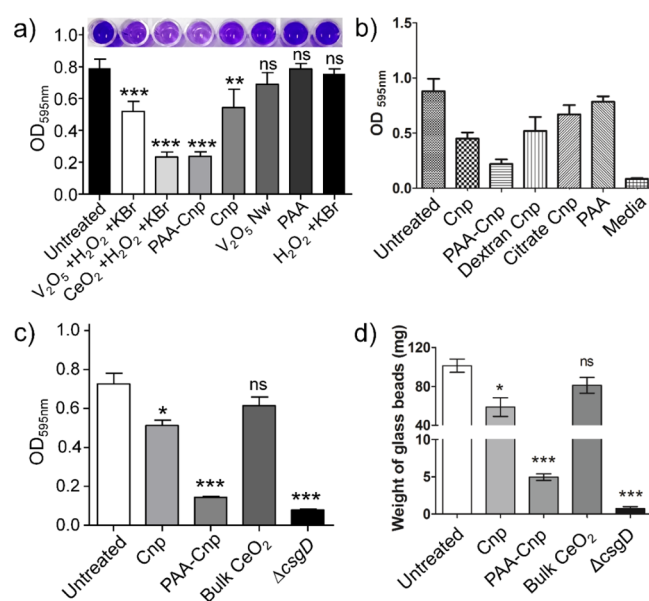


Figure 6. Comparison of biofilm inhibition property against *Salmonella* Typhimurium attributed by Cnp and PAA-Cnp. (a,b) Visualization and quantification of biofilm in various conditions by the CV staining assay. Bar diagram shows the comparison of biofilm formation between PAA-Cnp and haloperoxidase-mimetic nanozymes, V_2O_5 and CeO_2 , which were known antibiofouling agents as well as citrate- and dextran-coated Cnp, which were known antibacterial agents, respectively. (c) Bar diagram shows the quantification and comparison of biofilm formation among CeO_2 nanoparticles (Cnp), PAA-Cnp, and bulk form of CeO_2 . (d) Bar diagram shows the quantification of biofilm strength from the weight of glass bead held by the biofilms. One-way ANOVA with Bonferroni post-test was used to analyze the results. $P < 0.001 = ***$; $P < 0.01 = **$; $P < 0.05 = *$; and $P > 0.05 = \text{ns}$.

S24). All these results confirmed that biofilm inhibition by PAA-Cnp was exhibited independent of its haloperoxidase/oxidase activity.

The time-dependent analysis of the effect of PAA-Cnp treatment on *Salmonella* biofilm formation was done using confocal microscopy. Green fluorescent protein (GFP)-tagged *Salmonella* was cultured in the presence of nanozyme, PAA-Cnp, and the effect on biofilm formation was analyzed by staining the EPS matrix using Congo red dye at different time points for a period of 7 days.

We found the presence of more bacteria (green) embedded in the biofilm (red) in the case of PAA-Cnp-treated *Salmonella* compared with the untreated culture (Figure 7a). Further, the thickness of the biofilm was found to be significantly reduced (5-fold lesser) as compared to the untreated biofilm even after 7 days post-treatment (Figure 7b). We observed that both the biofilm-associated bacterial count (based on cfu) and EPS content around the bacterial cell colonies (based on dialysis) decreased in PAA-Cnp-treated cells compared to the untreated counterparts (Figure 7c,d). This further confirmed that the phospholipase-mimetic PAA-Cnp nanozyme could hamper the viability of bacteria and thus biofilm formation.

2.6. Scope and Utility Perspective of the Phospholipase-Mimetic Antibacterial Nanozymes. Phospholipids are ubiquitously present in the outer cell membrane, and thus, phospholipase-activity-based cell membrane hydrolysis can work as a global strategy to target a wide range of bacteria. To validate this, we checked the antibacterial activity of PAA-Cnp

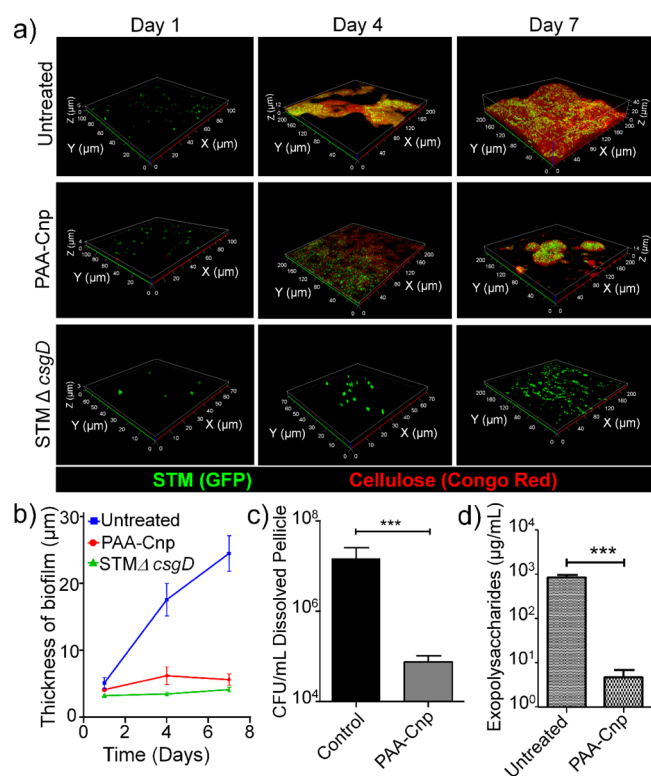


Figure 7. (a) Time-resolved monitoring of biofilm formation with or without treatment of PAA-Cnp using confocal microscopy. Congo red dye (red) and GFP-expressing *Salmonella* (green) were used to stain the EPS and bacteria, respectively. (b) Time-dependent measurement of biofilm formation was quantified from the thickness of z-axis of biofilm using confocal images. Note: *Salmonella* mutant Δ csgD (STM Δ csgD) which lacks transcription factor regulating biofilm formation was used as a negative control for all the experiments. (c) Bar diagram shows the quantification and comparison of *Salmonella* cfu from the biofilm grown in the presence or absence of PAA-Cnp. (d) Quantification of EPS content using dialysis of the biofilm pellicle from the *Salmonella* biofilm grown for 5 days in the presence or absence of PAA-Cnp. Student's *t* test was used to analyze the results. $P < 0.001 = ***$.

nanozyme on potential human pathogens *E. coli*, *S. Typhi*, *V. cholerae*, *S. flexneri*, and *K. pneumoniae* associated with chronic infections such as typhoid, cholera, dysentery, pneumonia, and so forth.⁶⁵

The dose- and time-dependent antibacterial activity of PAA-Cnp was determined using confocal microscopy and cfu analysis (Figures S25–S29). It was observed that less than 20% of the stationary-phase bacteria survived after 12 h of treatment with PAA-Cnp. The antibacterial concentration required to kill more than 80% of the bacteria was found in the range of 25–75 μ g/mL (Table 1). Thus, the novel phospholipase-like activity of nanoceria coated with PAA on the surface of the nanozyme favors spatiotemporal interaction with the lipophilic cell membrane showing global bactericidal effect.

According to a survey in 2011, urinary tract infections (UTIs) were among the most common type of healthcare-associated infections.⁶⁶ The widespread use of urinary catheterization in hospitals and long-term care facilities which happen to be the major source of UTI, also known as catheter-associated UTI (CAUTI), may lead to more severe complications, for example, sepsis and endocarditis, and so forth.⁶⁷ Pathogenic bacteria such as *Salmonella* and *S. aureus*

Table 1. Minimum Concentration of PAA-Cnp Required To Kill More Than 80% of Various Pathogenic Bacteria 12 h Postincubation

organism	concentration PAA-Cnp (μ g/mL)	percent killing after 12 h (mean \pm SD)
<i>Escherichia coli</i>	50	84 \pm 4
<i>Klebsiella pneumoniae</i>	50	90 \pm 2
<i>Salmonella Typhi</i>	75	88 \pm 3
<i>Vibrio cholerae</i>	25	80 \pm 1
<i>Shigella flexneri</i>	75	88 \pm 4

excreted through urine cause contamination of urinary catheters through biofilm formation using catheters as a substratum. Urinary catheters containing microbes on its surface cause the introduction of pathogenic bacteria in the urinary system resuscitating the urinary infection. Thus, for patients with urinary infections, the use of urinary catheters is a major requirement as well as a health concern.

We propose that the broad-spectrum antibacterial and antibiofilm activity of Cnp and PAA-Cnp can be employed against infections involving multiple bacteria such as UTIs. For this, the inner surface of the catheters was coated with our nanozymes (Cnp and PAA-Cnp) (Figure S30). Biofilm formation was compared with uncoated catheter surfaces using confocal microscopy. Decreased attachment of bacterial cells was observed on the surface of nanozyme-coated catheters as compared to the uncoated catheters (Figures 8a,b,e,f, and S32a). Correspondingly, a decrease in bacterial colonization

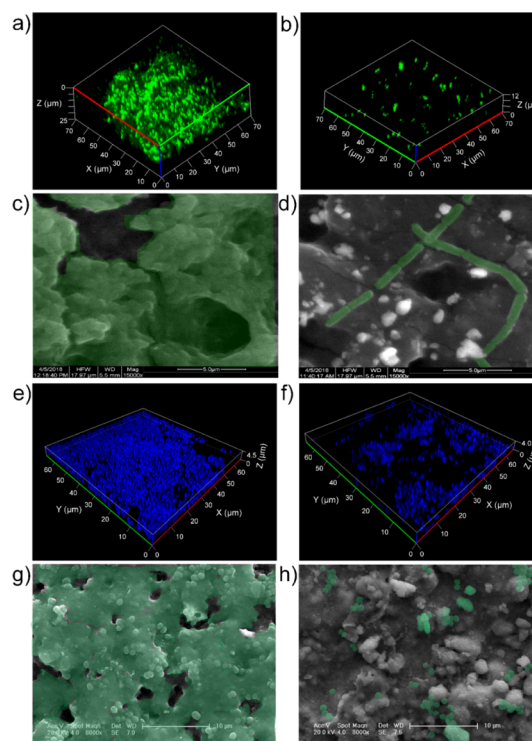


Figure 8. Representative confocal image and SEM images, respectively, of the biofilm formed by *Salmonella* (expressing GFP) on (a,c) uncoated catheter and (b and d) Cnp-coated catheter, whereas the biofilm formed by *S. aureus* (stained with DAPI) on (e and f) uncoated catheter and (g,h) Cnp-coated catheter. The bacterial biofilm or individual cells are highlighted with a green overlay in the SEM images (c,d and g,h).

was observed from the SEM images of the coated catheters as compared to uncoated catheters validating our earlier observation (Figures 8c,d,g,h, S31, and S32b). Further, it was noted that the catheters coated with Cnp showed better retention of the nanozyme on their surface (because of greater dispersibility of PAA-Cnp in solution), and therefore, less adherence of *Salmonella* and *S. aureus* bacterial cells was observed on these catheters compared with PAA-Cnp-coated catheters (Figures 8b and S32a). This implies that PAA-Cnp shows more potent antibacterial activity in water dispersion phase, but bare Cnp shows stronger adherence to the catheter surface and hence proves to be an effective antibacterial coating agent. Moreover, coating the surface of urinary catheter by phospholipase-mimetic Cnp nanozyme prevented preattachment and settlement of bacteria on the surface by hydrolyzing the bacterial cell membrane avoiding colonization, leading to an antibiofilm activity.

The novel phospholipase activity of ceria-based nanozyme explored in this work can be further optimized by suitable coating to improve the antibacterial activity and selectivity toward bacterial cells. This membrane disruption-based strategy will be useful for the development of antibacterial nanozymes so as to selectively target only harmful bacteria. As our Cnp and PAA-Cnp nanozymes target an integral structural component of the bacterial cell, that is, membrane phospholipids, development of such nanozyme-based compounds will prevent the risk of antibacterial resistance, which is a major drawback of the currently available β -lactam antibiotics.

3. CONCLUSIONS

In conclusion, we have successfully developed the first example of a phospholipase-mimetic ceria-based nanozyme that can hydrolyze cell membrane phospholipids. We unambiguously demonstrated the depolarization of the membrane potential and leakage of cellular genetic material, which is responsible for the remarkable inhibitory effect on bacterial growth in stationary-phase and biofilm formation as compared to that of known antibiofouling and antibacterial agents. Interestingly, the nanozyme was not only permeable to biofilm but also capable of targeting bacterial cells inside the biofilms, thereby making it more potent as compared to the conventional antibiotics, which are inaccessible to bacteria residing in the biofilm. The nanozyme shows potential effect on a wide range of human pathogens such as gastrointestinal pathogens (*E. coli*, *S. Typhi*, *V. cholerae*, and *S. flexneri*) and respiratory pathogens (*K. pneumoniae*) associated with chronic infections such as typhoid, cholera, dysentery, pneumonia, and so forth. Broad-spectrum phospholipase-mimetic nanozyme plays a potential role in preventing bacterial colonization and biofilm formation on the surface of urinary catheters, a major cause of the healthcare-associated UTIs. Further, suitable coating of nanoceria with more biocompatible agents can be useful for designing a potent phospholipase-mimetic ceria-based antibiotic nanozyme in the future.

4. EXPERIMENTAL SECTION

4.1. Synthesis of the Nanoparticles. **4.1.1. Synthesis Procedure for Cnp Nanoparticles (Cnp).** Cerium oxide nanoparticles were synthesized by a hydrothermal process as reported previously with slight modifications.⁴⁷ In a typical experiment, the salt of Ce(IV) ions was taken as a precursor, and its hydroxide formed by treating with mild base was heated at high temperature and pressure to generate the

nanoparticles. The nanoparticles were synthesized by taking 350 mg of ceric ammonium nitrate ((NH₄)₂Ce(NO₃)₆) (0.64 mmol) and dissolving it in 35 mL of deionized water. After stirring at 800 rpm for 10 min to obtain a homogeneous solution of the salt, ethylenediamine (105 μ L, 1.6 mmol) and hydrazine hydrate (91 μ L, 3 mmol) were added immediately and the reaction mixture was again stirred at 800 rpm for 10 min. Subsequently, it was transferred in a 50 mL Teflon-lined stainless steel autoclave and heated at 120 °C for 5 h in a heating oven under pressure. Once the reaction was over and the autoclave was cooled, the solid precipitate obtained was washed several times with deionized water by centrifugation (3700 rpm for 10 min) till the pH was neutral. Finally, the white precipitate obtained was washed with ethanol and dried at 60 °C for 24 h. The dried pale white solid was calcined at 500 °C for 1 h.

4.1.2. Synthesis Procedure for PAA-Cnp Nanoparticles. PAA-coated Cnp nanoparticles were synthesized by the chemical precipitation method according to the reported procedure with slight modifications.⁴⁶ In a typical experiment, 1.0 M cerium(III) nitrate hexahydrate (2.17 g, Ce(NO₃)₃·7H₂O) was dissolved in 5.0 mL of deionized water and mixed separately with an aqueous solution of 0.5 M sodium polyacrylate in deionized water by stirring at 1000 rpm for 12 h to form a homogeneous suspension. The resultant mixture was added to an ammonium hydroxide solution (30.0 mL, 30%) under stirring. The solution was continuously stirred for another 24 h at room temperature (25–30 °C). The preparation was then centrifuged at 4000 rpm for two 30 min cycles to settle any debris and large agglomerates. The supernatant solution was then purified from free polymers and other reagents and then concentrated using a 10K Amicon cell. The concentrated product was freeze-dried to obtain a yellow powder of PAA-Cnp nanoparticles.

4.1.3. Synthesis Procedure for FITC-Tagged PAA-Cnp Nanoparticles. PAA-Cnp nanoparticles were first functionalized with 3-aminopropyltriethoxysilane (APTES) by mixing PAA-Cnp (200 mg) with APTES (3 mL) in dimethylformamide (DMF) at room temperature (25–30 °C) under stirring at 1000 rpm for 24 h (modified from ref 70). The amino-functionalized PAA-coated nanoceria (NH₂-PAA-Cnp) was washed with DMF by centrifugation at 10,000 rpm for three 15 min cycle to purify it from free polymers. The centrifuged product (NH₂-PAA-Cnp, 4 mg) was then resuspended in 0.5 mL of DMF, mixed with 0.5 mL of 2 mg mL⁻¹ FITC in DMF, and stirred at room temperature (25–30 °C) for 12 h. The orange product of FITC-tagged PAA-Cnp nanoparticles was purified from free polymers by washing thrice with acetone and then with water until the supernatant was clear and centrifuged at 10,000 rpm for 15 min.

4.2. Study of in Vitro Phospholipase Activity of the Nanoparticles. **4.2.1. Analysis of PPG Hydrolysis by Cnp and PAA-Cnp by MALDI Analysis.** The stock solution of nanocatalysts (2.0 mg/mL) was sonicated with a probe sonicator using 30% amplitude for 30 min at a 5–5 s on–off pulse. Hydrolysis was carried out by reacting 100 μ g/mL of nanocatalyst with 1.0 mM PPG in 50 mM Tris buffer pH 7.8. The reaction was performed in a 2.0 mL Eppendorf vial placed on a continuously stirring water bath maintained at 37 °C. After the reaction was carried out for a specific time period, the reaction was quenched by centrifugation of the reaction mixture at 10,000 rpm for 30 min. The supernatant was collected and analyzed by MALDI-Mass.

4.2.2. Comparison of PLC versus PLD Activity of Cnp and PAA-Cnp Nanocatalysts by the Red Chromogen Dye-Based UV–Vis Assay. Hydrolysis was carried with 100 μ g/mL of nanocatalyst taken from the stock solution of nanocatalysts (2.0 mg/mL) prepared by sonication with a probe sonicator similar to previously used conditions.⁵⁰ In a typical experiment, hydrolysis of 1.0 mM PC (lecithin) was carried out by the nanocatalyst in 50 mM Tris buffer pH 7.8 kept in a 2.0 mL Eppendorf vial placed on a continuously stirring water bath maintained at 37 °C. After the reaction was carried out for a specific time period, the reaction was quenched by centrifugation of the reaction mixture at 10,000 rpm for 30 min. The supernatant containing the hydrolyzed product was collected and analyzed for red-chromogen dye formation using the combination of

enzymes, that is, ALP (25 units/mL), choline oxidase (5.0 units/mL), peroxidase (15.0 units/mL), and dye components 2-hydroxy-3,5-dichlorobenzene sulfonic acid sodium salt (HDCBS, 50.0 mM) and 4-aminoantipyrene (AAP, 15.0 mM) under the following different conditions.

4.2.2.1. PLC-Based Hydrolysis Assay. The supernatant containing the hydrolyzed product was analyzed for red-chromogen dye formation using the combination of all three enzymes, that is, ALP (25 units/mL), choline oxidase (5.0 units/mL), and peroxidase (15.0 units/mL), which convert choline phosphate to betaine and H₂O₂. Hydroxyl radicals generated from H₂O₂ by peroxidase react with HDCBS (50.0 mM) and AAP (15.0 mM) to form the red azo-dye after 30 min of incubation at 37 °C. The azo-dye was analyzed by a UV–vis spectrophotometer by observing the wavelength at 510 nm after 5 times dilution of the product using deionized water.

4.2.2.2. PLD-Based Hydrolysis Assay. The supernatant containing the hydrolyzed product was analyzed for red-chromogen dye formation using the combination of two enzymes, that is, choline oxidase (5.0 units/mL) and peroxidase (15.0 units/mL), which convert choline phosphate to betaine and H₂O₂. Hydroxyl radicals generated from H₂O₂ by peroxidase react with HDCBS (50.0 mM) and AAP (15.0 mM) to form the red azo-dye after 30 min of incubation at 37 °C. The azo-dye was analyzed by a UV–vis spectrophotometer by observing the wavelength at 510 nm after 5 times dilution of the product using deionized water.

4.2.2.3. Control Experiments. In one control experiment, the supernatant containing the hydrolyzed product was analyzed for red-chromogen dye formation in the absence of either of the two enzymes, that is, choline oxidase (5.0 units/mL) or peroxidase (15.0 units/mL), with the presence of dye components HDCBS (50.0 mM) and AAP (15.0 mM). In another control experiment, the supernatant containing the hydrolyzed product was analyzed for red-chromogen dye formation using the three enzymes, that is, ALP (25.0 units/mL), choline oxidase (5.0 units/mL), and peroxidase (15.0 units/mL), in the absence of dye components HDCBS (50.0 mM) and AAP (15.0 mM). The UV–vis spectra were recorded after a 30 min incubation of the enzyme and/or dye components at 37 °C after 5 times dilution of the product using deionized water.

4.2.3. PLC Activity Assay Using the NPPC Substrate. In all the cases mentioned below, the stock solution of nanocatalysts (2.0 mg/mL) was prepared by sonication with a probe sonicator similar to previously used conditions, using 30% amplitude for 30 min at a 5–5 s on–off pulse.

4.2.3.1. Monitoring the Formation of *p*-Nitrophenol by UV–Vis. The hydrolysis reaction of 10.0 mM NPPC was carried out using 100 µg/mL of nanocatalyst in 50 mM Tris buffer pH 7.8 kept in a 2.0 mL Eppendorf vial placed on a continuously stirring water bath maintained at 37 °C. Samples were collected at three different time points for each of the two nanocatalysts (Cnp and PAA-Cnp), that is, 6, 12, and 18 h. The peak for the hydrolyzed product, *p*-nitrophenol, at 405 nm was monitored by UV–vis spectroscopy after 5 times dilution of the product using deionized water. For comparison with substrate, the UV–vis spectra of 0.1 mM NPPC were recorded in the same wavelength range.

4.2.3.2. Initial Rate Comparison and Time Course Hydrolysis Study by UV–Vis. In a typical experiment, 10.0 mM NPPC was taken with the nanocatalyst (100 µg/mL) in 50.0 mM Tris buffer pH 7.8 kept in the quartz cuvette maintained at 37 °C. Two control experiments were performed, that is, (1) in the absence of any catalyst and (2) in the presence of PAA in the form of a catalyst. The UV spectrometer wavelength was fixed at 405 nm, and the hydrolysis was monitored at 3 min interval for 2 h. The initial rate in the first 30 min of hydrolysis was used for comparing the initial rates of the different nanocatalysts and control experiments. After 2 h, the hydrolysis time points were measured by carrying out the reaction in a 2.0 mL Eppendorf vial placed on a continuously stirring water bath maintained at 37 °C. The peak for the hydrolyzed product, *p*-nitrophenol, at 405 nm was monitored by UV–vis spectroscopy after 5 times dilution of the product using deionized water. The absorbance value of *p*-nitrophenol at the time point of 2 h was used as a reference

for normalization based on the difference in the experimental technique used for monitoring the hydrolysis.

4.2.3.3. Hydrolysis of NPPC by Different Concentrations of PAA-Cnp. In a typical experiment, 4.0 mM NPPC was taken, and four different sets of hydrolysis were carried out with separately four different concentrations of PAA-Cnp (100, 200, 350, and 500 µg/mL) in 50.0 mM Tris buffer pH 7.8 kept in a quartz cuvette maintained at 37 °C. The UV spectrometer wavelength was fixed at 405 nm, and the hydrolysis was monitored at 3 min interval for 2 h. The initial rate in the first 30 min of hydrolysis was used for comparing the initial rate in each of the four cases.

4.2.3.4. Michaelis–Menten Kinetics of NPPC Hydrolysis by Cnp and PAA-Cnp. In a typical experiment, 100 µg/mL of nanocatalyst was taken in 50.0 mM Tris buffer pH 7.8 kept in a quartz cuvette maintained at 37 °C, and different concentrations of NPPC were used, each concentration taken separately. Hydrolysis was monitored by observing the increase in the formation of *p*-nitrophenol in a UV spectrophotometer fixed at a wavelength of 405 nm at 3 min interval for 2 h. Michaelis–Menten and Lineweaver–Burk graphs were plotted between initial rate and different concentrations of NPPC for both the nanocatalysts.

4.2.3.5. Hydrolysis of NPPC by Cnp and PAA-Cnp Monitored by ³¹P NMR Spectroscopy. The hydrolysis reaction of 1.0 mM NPPC was carried out using 100 µg/mL of nanocatalyst in 50 mM Tris buffer pH 7.8 kept in a 2.0 mL Eppendorf vial placed on a continuously stirring water bath maintained at 37 °C. Samples were collected at three different time points for each of the two nanocatalysts (Cnp and PAA-Cnp), that is, 0.5, 6, and 48 h. The products of hydrolysis were analyzed using ³¹P NMR spectroscopy by taking 0.4 mL of supernatant of the centrifuged reaction mixture and recording the spectra for 500 scans at a 5.0 s delay time in the presence of DMSO-*d*₆ as an external standard and H₃PO₄ peak at 0.0 ppm as a standard for reference.

4.3. Bacterial Strains and Growth Media Used in the Study.

S. enterica subspecies *enterica* serovar Typhimurium strain ATCC 14028S wild type and *Salmonella* expressing GFP were plated either on LB medium or on LB supplemented with ampicillin (50 µg/mL). *Salmonella* mutant Δ*csdG* was grown on LB containing 20 µg/mL of chloramphenicol. Plating onto *Salmonella*–*Shigella* agar (SS agar), a semiselective differential medium, was used to determine *S. Typhimurium* as and when required. *E. coli* K-12 (Str. MG1655; ATCC 700926), *S. flexneri* (MTCC 1457), *V. cholerae* (MTCC 3904), *S. enterica* serovar Typhi (CT18; clinical isolate from PGI, Chandigarh, India), and *K. pneumoniae* (MTCC 618) were grown on LB broth at 37 °C or plated on LB agar. LB broth or M9 minimal media supplemented with 0.05% glucose as a carbon source was used to plot growth curve and death curve of bacteria. MIC for Cnp and PAA-Cnp was measured by growing *Salmonella* in M9 minimal media with 0.3% glucose. The cfu analysis was done on either SS agar (for *S. Typhimurium* and Typhi, *S. flexneri*, and *E. coli*) or LB agar (for *K. pneumoniae* and *V. cholerae*).

4.4. Confocal Microscopy and Image Analysis.

S. Typhimurium was used to form a biofilm. The slanting glass slides were washed thrice with sterile phosphate-buffered saline (PBS) and dipped in 4% paraformaldehyde for 30 min. It was washed again with sterile PBS. The extracellular polysaccharide was stained with Congo red dye (1 µg/mL) for 30 min. The glass slides were washed and dried. These were mounted over a glass coverslip and image was acquired using a confocal microscope. For live dead bacterial analysis, PI (0.01 µg/mL) was used to stain the bacterial smear on the coverslip. After washing the excess stain with PBS, the cells were counterstained with DAPI (0.1 µg/mL). The cells which were dual positive for DAPI and PI were considered dead. For visualization of live and dead cells from the biofilm, the entire biofilm was mechanically disrupted by beading and cells were stained with PI, followed by DAPI. The cells were then spin down. Because PI has nonspecific affinity toward cellulose, a cellulosic film was used as a control to adjust the laser power and minimize the background and nonspecific fluorescence from the biofilm matrix. Cells positive for DAPI and PI were considered dead cells.

For estimating the membrane potential of the bacteria, 1 $\mu\text{g}/\text{mL}$ of Di-BAC₄(3) was used to stain the bacterial cells for 40 min at 37 °C.

Log-phase and stationary-phase grown *Salmonella* treated with ampicillin or CTAB, respectively, were used as positive control for membrane depolarization.

For visualizing the DNA release from bacterial cells, 0.1 $\mu\text{g}/\text{mL}$ of DAPI was used and the cell membrane was stained by FM4-64 (0.1 $\mu\text{g}/\text{mL}$ for 30 min). Image acquisition of the biofilm was done using a Zeiss confocal microscope (LSM Meta 710). Three-dimensional (3D) reconstitution of biofilm was done using the ZEN Blue 2012 platform.

4.5. Growth Stage-Based Antibacterial Activity. Overnight grown cultures of *S. Typhi* CT18 and *E. coli* TG1 were subcultured in 1:100 ratio in M9 minimal media with or without the nanoparticles and ciprofloxacin (5 $\mu\text{g}/\text{mL}$). The growth of the bacteria was checked at every 2 h by taking the optical density (OD) at 595 nm, and cfu was determined by dilution plating. MIC determination was done based on the broth dilution assay as per the CLSI guidelines.^{68,69} Initial cfu and cfu after 12 h of the culture were also determined. The fold proliferation of the bacteria was measured as the ratio of cfu at 12 h to cfu at 0 h. The MIC of PAA-Cnp, Cnp, Ag nanoparticles, and ciprofloxacin as antibiotic control were done for *S. Typhi* and *E. coli*. Varying range of nanoparticle concentrations, 5–500 $\mu\text{g}/\text{mL}$, was used for MIC determination.

Growth and death curves of *Salmonella* were plotted in LB broth containing 50 $\mu\text{g}/\text{mL}$ of PAA-Cnp and Cnp. For growth curve, 50 μL of overnight culture was used as inoculum, and cfu was monitored at different time points. Concomitantly, pregrown bacterial culture (stationary phase) was treated with 50 $\mu\text{g}/\text{mL}$ of PAA-Cnp or Cnp, and cfu was plotted over time to plot the death curve. M9 media containing 0.05% glucose, pretreated with PAA-Cnp or Cnp, was also used to analyze the antibacterial effect. A lower amount of glucose was used to attain a quick stationary phase. Visualization of dead bacteria was done at log and stationary phase by staining the cells with PI and DAPI and observed under a confocal microscope.

4.6. HeLa Cell Viability Check by the MTT Assay. Around 25,000 HeLa cells (ATCC CCL-2) were seeded in duplicates in each well of 96-well plates. The cells were incubated overnight in complete media (Dulbecco's modified Eagle's medium + 10% fetal bovine serum) for attachment to the plate. After 12 h, different nanoparticles were added in each well. The cells were incubated for different time points, 2, 6, 9, 12, and 72 h, with the nanoparticles. After each incubation, 10 μL of MTT (stock 5 mg/mL in PBS) was added to each well and incubated at 37 °C with 5% CO₂ for 4 h. Next, the media was removed from each well, and 100 μL of dimethyl sulfoxide was added to solubilize the formazan dye. The plate was incubated for 1 h at 37 °C, and the OD was measured at 570 nm.

4.7. Biofilm Formation and Quantification. The pellicle and the submerged biofilm were allowed to form in 24-well microtiter plates. LB media (2 mL, without NaCl) was dispensed in the wells and inoculated with 10⁷ cells (*S. Typhimurium*) from an overnight culture. Nanoparticles (50 $\mu\text{g}/\text{mL}$) were added to each well. The microtiter plates were incubated under static condition for 5 days at 28 °C. The wells were washed thrice with PBS and the biofilm was stained with 1% CV dye solution for 15 min, and again the wells were rinsed thrice with PBS to wash off the unbound dye. Quantification of the biofilm biomass was done by destaining the CV with absolute ethanol and recording the absorbance at 595 nm. The strength of the air–liquid interface biofilm was quantified by enumerating the weight of the glass bead it can hold before breaking.

4.8. Biocidal Activity against Various Pathogenic Bacteria. Different concentrations of PAA-Cnp and Cnp were suspended in 10 mL of PBS (1 \times) containing 10⁷ cfu /mL of *S. Typhi*, *E. coli*, *V. cholerae*, and *K. pneumoniae*. Survival was measured by plating and enumerating cfu expressed in percentage, [(cfu t_n /cfu t_0) \times 100], where cfu t_n represents cfu at any given time after nanoparticle treatment and cfu t_0 represents cfu immediately after nanoparticle treatment. Aliquots were taken at every time point and stained with PI (0.01 $\mu\text{g}/\text{mL}$ for 10 min) to visualize the dead cells. The bacterial cells were post-stained with DAPI (0.1 $\mu\text{g}/\text{mL}$ for 10 min) and

observed under a confocal microscope LSM 710 Meta with 100 \times objective.

4.9. Biofilm Formation in the Inner Surface of Urinary Catheters. Sections (5 mm \times 5 mm) of urinary catheters were cut and coated with either Cnp or PAA Cnp. These coated catheters were dipped in the biofilm forming media for 5 days. After incubation, these catheters were washed with sterile 1 \times PBS and imaged using either confocal microscopy or SEM. For confocal microscopy, DAPI staining was done for *S. aureus*. For *S. Typhimurium*, no post-staining was done as the strain was expressing GFP. Images were acquired using Zeiss LSM 710 Meta and analyzed using the ZEN 2012 platform. SEM and glutaraldehyde fixation were done overnight, followed by serial dehydration and vacuum-drying. Gold coating was done using the JOEL-JFC-1100E ion sputtering device, observed under a scanning electron microscope, and analyzed by field emission SEM (FEI Sirion, Eindhoven, The Netherlands).

■ ASSOCIATED CONTENT

Supporting Information

The Supporting Information is available free of charge at <https://pubs.acs.org/doi/10.1021/acsabm.0c00363>.

Characterization of nanozymes; phospholipase-like activity of nanozymes; representation of phospholipase-like activity on the nanoceria surface; confocal microscopy studies on cell membrane damage studies; antibacterial activity studies; FITC-tagged nanozyme synthesis, characterization, and cellular localization studies; dispersibility of nanozymes; biofilm inhibition studies; PI staining assay to study the antibacterial activity of nanozymes on different pathogenic bacteria; antibiofouling activity on urinary catheters; and cytotoxicity studies of nanozymes (PDF)

■ AUTHOR INFORMATION

Corresponding Authors

Dipshikha Chakravorty – Department of Microbiology and Cell Biology and Center for Biosystems Science and Engineering, Indian Institute of Science, Bangalore 560012, India; Email: dipa@iisc.ac.in

Govindasamy Mugesh – Department of Inorganic and Physical Chemistry, Indian Institute of Science, Bangalore 560012, India; orcid.org/0000-0002-5389-5309; Email: mugesh@iisc.ac.in

Authors

Kritika Khulbe – Department of Inorganic and Physical Chemistry, Indian Institute of Science, Bangalore 560012, India

Kapudeep Karmakar – Department of Microbiology and Cell Biology, Indian Institute of Science, Bangalore 560012, India; Regional Research Station, Terai Zone, Uttar Banga Krishi Viswavidyalaya-ICAR, Coochbehar 736165, West Bengal, India

Sourav Ghosh – Department of Inorganic and Physical Chemistry, Indian Institute of Science, Bangalore 560012, India

Kasturi Chandra – Department of Microbiology and Cell Biology, Indian Institute of Science, Bangalore 560012, India

Complete contact information is available at:

<https://pubs.acs.org/doi/10.1021/acsabm.0c00363>

Author Contributions

Kritika Khulbe and Kapudeep Karmakar contributed equally. The manuscript was written through contributions of all authors. All authors have given approval to the final version of the manuscript.

Notes

The authors declare no competing financial interest.

ACKNOWLEDGMENTS

This study was supported by the DST Nano Mission (SR/NM/NS-1380/2014), DST, New Delhi. G.M. acknowledges the SERB/DST for the award of J. C. Bose National Fellowship (SB/S2/JCB-067/2015). D.C. is supported by ASTRA-Chair and DAE-SRC outstanding research fellowships. D.C. acknowledges the DBT-IISc partnership programme, the Centre of Advanced Studies (UGC), the DST FIST level II infrastructure support, the departmental Confocal Microscopy, and the divisional Bioimaging/SEM facilities. Kritika Khulbe, Kapudeep Karmakar, S.G., and K.C. thank the Indian Institute of Science, Bangalore, for the fellowship (from MHRD, Government of India), AFMM and MNCF Facility, CeNSE, IISc, for the spectroscopic and microscopic facilities. Kritika Khulbe thanks Punarbasu Roy and Sarath Babu B.N. for extending help in some of the experiments. Kapudeep Karmakar thanks the confocal facility in the Department of Microbiology and Cell Biology, Biological Sciences Divisional Bioimaging/SEM facility as well as Anusha, Divya, Saima, and Satyawati for helping in the acquisition of images.

ABBREVIATIONS

Cnp, CeO₂ nanoparticles; PAA-Cnp, PAA-coated CeO₂ nanoparticles; PLC, phospholipase C; PLD, phospholipase D; NPPC, *p*-nitrophenyl phosphatidylcholine; POPG, 1-palmitoyl-2-oleoyl-*sn*-glycero-3-phosphoglycerol; HDCBS, 2-hydroxy-3,5-dichlorobenzene sulfonic acid; AAP, 4-aminoantipyrene; ALP, alkaline phosphatase; ChOx, choline oxidase; PerOx, peroxidase; LB, Luria broth; DAPI, 4',6-diamidino-2-phenylindole; FITC, fluorescein isothiocyanate; FM4-64, *N*-(3-triethylammoniumpropyl)-4-(6-(4-(diethylamino)phenyl)hexatrienyl)pyridiniumdibromide

REFERENCES

- 1) <https://www.nobelprize.org/prizes/medicine/1945/summary>. The Nobel Prize in Physiology or Medicine 1945 (October 2019).
- 2) Levy, S. B.; Marshall, B. Antibacterial Resistance Worldwide: Causes, Challenges and Responses. *Nat. Med.* **2004**, *10*, S122–S129.
- 3) News published in <https://www.who.int/news-room/detail/21-09-2016-at-un-global-leaders-commit-to-act-on-antimicrobial-resistance> (October 2019).
- 4) Ford, C.; Zurenko, G.; Barbachyn, M. The Discovery of Linezolid, the First Oxazolidinone Antibacterial Agent. *Curr. Drug Targets: Infect. Disord.* **2001**, *1*, 181–199.
- 5) LaPlante, K. L.; Rybak, M. J. Daptomycin – A Novel Antibiotic Against Gram-positive Pathogens. *Expert Opin. Pharmacother.* **2004**, *5*, 2321–2331.
- 6) Brown, E. D.; Wright, G. D. New Targets and Screening Approaches in Antimicrobial Drug Discovery. *Chem. Rev.* **2005**, *105*, 759–774.
- 7) Whitchurch, C. B.; Nielsen, T. T.; Ragas, P. C.; Mattick, J. S. Extracellular DNA Required for Bacterial Biofilm Formation. *Science* **2002**, *295*, 1487.
- 8) Chen, Z.; Wang, Z.; Ren, J.; Qu, X. Enzyme Mimicry for Combating Bacteria and Biofilms. *Acc. Chem. Res.* **2018**, *51*, 789–799.
- 9) Xu, J.-W.; Yao, K.; Xu, Z.-K. Nanomaterials with a Photothermal Effect for Antibacterial Activities: An Overview. *Nanoscale* **2019**, *11*, 8680–8691.
- 10) Ma, S.; Zhan, S.; Jia, Y.; Zhou, Q. Superior Antibacterial Activity of Fe₃O₄-TiO₂ Nanosheets under Solar Light. *ACS Appl. Mater. Interfaces* **2015**, *7*, 21875–21883.

- 11) Hu, M.; Chen, J.; Li, Z.-Y.; Au, L.; Hartland, G. V.; Li, X.; Marquez, M.; Xia, Y. Gold Nanostructures: Engineering Their Plasmonic Properties for Biomedical Applications. *Chem. Soc. Rev.* **2006**, *35*, 1084–1094.
- 12) Sun, H.; Gao, N.; Dong, K.; Ren, J.; Qu, X. Graphene Quantum Dots-Band-Aids Used for Wound Disinfection. *ACS Nano* **2014**, *8*, 6202–6210.
- 13) Natalio, F.; André, R.; Hartog, A. F.; Stoll, B.; Jochum, K. P.; Wever, R.; Tremel, W. Vanadium Pentoxide Nanoparticles Mimic Vanadium Haloperoxidases and Thwart Biofilm Formation. *Nat. Nanotechnol.* **2012**, *7*, 530–535.
- 14) Herget, K.; Hubach, P.; Pusch, S.; Deglmann, P.; Götz, H.; Gorelik, T. E.; Gural'skiy, I. y. A.; Pftzner, F.; Link, T.; Schenk, S.; Panthöfer, M.; Ksenofontov, V.; Kolb, U.; Opatz, T.; André, R.; Tremel, W. Haloperoxidase Mimicry by CeO_{2-x} Nanorods Combats Biofouling. *Adv. Mater.* **2017**, *29*, 1603823.
- 15) Chen, Z.; Ji, H.; Liu, C.; Bing, W.; Wang, Z.; Qu, X. A Multinuclear Metal Complex Based DNase-Mimetic Artificial Enzyme: Matrix Cleavage for Combating Bacterial Biofilms. *Angew. Chem., Int. Ed.* **2016**, *55*, 10732–10736.
- 16) Zhao, Y.; Tian, Y.; Cui, Y.; Liu, W.; Ma, W.; Jiang, X. Small Molecule-Capped Gold Nanoparticles as Potent Antibacterial Agents That Target Gram-Negative Bacteria. *J. Am. Chem. Soc.* **2010**, *132*, 12349–12356.
- 17) Wang, B.; Pachaiyappan, B.; Gruber, J. D.; Schmidt, M. G.; Zhang, Y.-M.; Woster, P. M. Antibacterial Diamines Targeting Bacterial Membranes. *J. Med. Chem.* **2016**, *59*, 3140–3151.
- 18) Ben-Knaz Wakshlak, R. B.; Pedahzur, R.; Avnir, D. Antibacterial Activity of Silver-killed Bacteria: The "Zombies" Effect. *Sci. Rep.* **2015**, *5*, 9555.
- 19) Swathy, J. R.; Sankar, M.; Chaudhary, A.; Aigal, S.; Anshup; Pradeep, T. Antimicrobial Silver: An Unprecedented Anion Effect. *Sci. Rep.* **2015**, *4*, 7161.
- 20) Jung, W. K.; Koo, H. C.; Kim, K. W.; Shin, S.; Kim, S. H.; Park, Y. H. Antibacterial Activity and Mechanism of Action of the Silver Ion in *Staphylococcus aureus* and *Escherichia coli*. *Appl. Environ. Microbiol.* **2008**, *74*, 2171–2178.
- 21) Coates, A.; Hu, Y.; Bax, R.; Page, C. The Future Challenges Facing the Development of New Antimicrobial Drugs. *Nat. Rev. Drug Discovery* **2002**, *1*, 895–910.
- 22) Flemming, H.-C.; Wingender, J. The Biofilm Matrix. *Nat. Rev. Microbiol.* **2010**, *8*, 623–633.
- 23) Buhmann, M. T.; Stiefel, P.; Maniura-Weber, K.; Ren, Q. In Vitro Biofilm Models for Device-Related Infections. *Trends Biotechnol.* **2016**, *34*, 945–948.
- 24) Ojha, A. K.; Baughn, A. D.; Sambandan, D.; Hsu, T.; Trivelli, X.; Guerardel, Y.; Alahari, A.; Kremer, L.; Jacobs, W. R.; Hatfull, G. F. Growth of *Mycobacterium tuberculosis* Biofilms Containing Free Mycolic Acids and Harboring Drug-tolerant Bacteria. *Mol. Microbiol.* **2008**, *69*, 164–174.
- 25) Lee, H.-W.; Koh, Y. M.; Kim, J.; Lee, J.-C.; Lee, Y.-C.; Seol, S.-Y.; Cho, D.-T.; Kim, J. Capacity of Multidrug-resistant Clinical Isolates of *Acinetobacter baumannii* to Form Biofilm and Adhere to Epithelial Cell Surfaces. *Clin. Microbiol. Infect.* **2008**, *14*, 49–54.
- 26) Costerton, J. W.; Cheng, K. J.; Geesey, G. G.; Ladd, T. I.; Nickel, J. C.; Dasgupta, M.; Marrie, T. J. Bacterial Biofilms in Nature and Disease. *Annu. Rev. Microbiol.* **1987**, *41*, 435–464.
- 27) Schultz, D.; Onuchic, J. N.; Ben-Jacob, E. Turning Death into Creative Force During Biofilm Engineering. *Proc. Natl. Acad. Sci. U.S.A.* **2012**, *109*, 18633–18634.
- 28) Hall-Stoodley, L. H.; Costerton, J. W.; Stoodley, P. Bacterial Biofilms: From the Natural Environment to Infectious Diseases. *Nat. Rev. Microbiol.* **2004**, *2*, 95–108.
- 29) Lewis, K. Persister Cells. *Annu. Rev. Microbiol.* **2010**, *64*, 357–372.
- 30) Donlan, R. M.; Costerton, J. W. Biofilms: Survival Mechanisms of Clinically Relevant Microorganisms. *Clin. Microbiol. Rev.* **2002**, *15*, 167–193.

- (31) Govan, J. R.; Deretic, V. Microbial Pathogenesis in Cystic Fibrosis: Mucoid *Pseudomonas aeruginosa* and *Burkholderia cepacia*. *Microbiol. Rev.* **1996**, *60*, 539–574.
- (32) Feigin, R. D.; Cherry, J. D. *Otitis Media in Textbook of Pediatric Infectious Diseases*; Feigin, R. D., Kline, M. W., Hyatt, S. R., Ford, K. L., Eds.; W. B. Saunders Co., Philadelphia, 1992; Vol. 164; pp 174–189.
- (33) Alpaslan, E.; Geilich, B. M.; Yazici, H.; Webster, T. J. pH-Controlled Cerium Oxide Nanoparticle Inhibition of Both Gram-Positive and Gram-Negative Bacteria Growth. *Sci. Rep.* **2017**, *7*, 45859.
- (34) Thill, A.; Zeyons, O.; Spalla, O.; Chauvat, F.; Rose, J.; Auffan, M.; Flank, A. M. Cytotoxicity of CeO₂ Nanoparticles for *Escherichia coli*. Physico-chemical Insight of the Cytotoxicity Mechanism. *Environ. Sci. Technol.* **2006**, *40*, 6151–6156.
- (35) Pelletier, D. A.; Suresh, A. K.; Holton, G. A.; McKeown, C. K.; Wang, W.; Gu, B.; Mortensen, N. P.; Allison, D. P.; Joy, D. C.; Allison, M. R.; Brown, S. D.; Phelps, T. J.; Doktycz, M. J. Effects of Engineered Cerium Oxide Nanoparticles on Bacterial Growth and Viability. *Appl. Environ. Microbiol.* **2010**, *76*, 7981–7989.
- (36) Fang, X.; Yu, R.; Li, B.; Somasundaran, P.; Chandran, K. Stresses Exerted by ZnO, CeO₂ and Anatase TiO₂ Nanoparticles on the *Nitrosomonas europaea*. *J. Colloid Interface Sci.* **2010**, *348*, 329–334.
- (37) Tso, C.-p.; Zhung, C.-m.; Shih, Y.-h.; Tseng, Y.-M.; Wu, S.-c.; Doong, R.-a. Stability of Metal Oxide Nanoparticles in Aqueous Solutions. *Water Sci. Technol.* **2010**, *61*, 127–133.
- (38) Shah, V.; Shah, S.; Shah, H.; Rispoli, F. J.; McDonnell, K. T.; Workeneh, S.; Karakoti, A.; Kumar, A.; Seal, S. Antibacterial Activity of Polymer Coated Cerium Oxide Nanoparticles. *PLoS One* **2012**, *7*, No. e47827.
- (39) Scher, K.; Romling, U.; Yaron, S. Effect of Heat, Acidification, and Chlorination on *Salmonella enterica* Serovar Typhimurium Cells in a Biofilm Formed at the Air-Liquid Interface. *Appl. Environ. Microbiol.* **2005**, *71*, 1163–1168.
- (40) Hung, C.; Zhou, Y.; Pinkner, J. S.; Dodson, K. W.; Crowley, J. R.; Heuser, J.; Chapman, M. R.; Hadjifrangiskou, M.; Henderson, J. P.; Hultgren, S. J. *Escherichia coli* Biofilms Have an Organized and Complex Extracellular Matrix Structure. *mBio* **2013**, *4*, No. e00645.
- (41) Manto, M. J.; Xie, P.; Wang, C. Catalytic Dephosphorylation Using Ceria Nanocrystals. *ACS Catal.* **2017**, *7*, 1931–1938.
- (42) Wang, Z.-G.; Bi, W.-Z.; Ma, S.-C.; Lv, N.; Zhang, J.-L.; Sun, D.-H.; Ni, J.-Z. Facet-Dependent Effect of Well-Defined CeO₂ Nanocrystals on the Adsorption and Dephosphorylation of Phosphorylated Molecules. *Part. Part. Syst. Char.* **2015**, *32*, 652–660.
- (43) Vernekar, A. A.; Das, T.; Mughesh, G. Vacancy-Engineered Nanoceria: Enzyme Mimetic Hotspots for the Degradation of Nerve Agents. *Angew. Chem., Int. Ed.* **2016**, *55*, 1412–1416.
- (44) Xu, C.; Qu, X. Cerium Oxide Nanoparticle: A Remarkably Versatile Rare Earth Nanomaterial for Biological Applications. *NPG Asia Mater.* **2014**, *6*, No. e90.
- (45) Tan, F.; Zhang, Y.; Wang, J.; Wei, J.; Cai, Y.; Qian, X. An Efficient Method for Dephosphorylation of Phosphopeptides by Cerium Oxide. *J. Mass Spectrom.* **2008**, *43*, 628–632.
- (46) Asati, A.; Santra, S.; Kaittanis, C.; Perez, J. M. Surface-Charge-Dependent Cell Localization and Cytotoxicity of Cerium Oxide Nanoparticles. *ACS Nano* **2010**, *4*, 5321–5331.
- (47) Panahi-Kalamuei, M.; Alizadeh, S.; Kamazani, M. M.; Niasari, M. S. Synthesis and Characterization of CeO₂ Nanoparticles via Hydrothermal Route. *J. Ind. Eng. Chem.* **2015**, *21*, 1301–1305.
- (48) Todica, M.; Stefan, R.; Pop, C. V.; Olar, L. IR and Raman Investigation of Some Poly(acrylic) Acid Gels in Aqueous and Neutralized State. *Acta Phys. Pol.* **2015**, *128*, 128–135.
- (49) Maniego, A. R.; Sutton, A. T.; Guillaneuf, Y.; Lefay, C.; Destarac, M.; Fellows, C. M.; Castignolles, P.; Gaborieau, M. Degree of Branching in Poly(acrylic acid) Prepared by Controlled and Conventional Radical Polymerization. *Polym. Chem.* **2019**, *10*, 2469–2476.
- (50) Hergenrother, P. J.; Spaller, M. R.; Haas, M. K.; Martin, S. F. Chromogenic Assay for Phospholipase C from *Bacillus cereus*. *Anal. Biochem.* **1995**, *229*, 313–316.
- (51) Bêche, E.; Charvin, P.; Perarnau, D.; Abanades, S.; Flamant, G. Ce 3d XPS Investigation of Cerium Oxides and Mixed Cerium Oxide (CexTiyOz). *Surf. Interface Anal.* **2008**, *40*, 264–267.
- (52) Naganuma, T.; Traversa, E. Air, Aqueous and Thermal Stabilities of Ce³⁺ Ions in Cerium Oxide Nanoparticle Layers with Substrates. *Nanoscale* **2014**, *6*, 6637–6645.
- (53) Korsvik, C.; Patil, S.; Seal, S.; Self, W. T. Superoxide Dismutase Mimetic Properties Exhibited by Vacancy Engineered Ceria Nanoparticles. *Chem. Commun.* **2007**, 1056–1058.
- (54) Baudin, M.; Wójcik, M.; Hermansson, K. Dynamics, Structure and Energetics of the (111), (011) and (001) Surfaces of Ceria. *Surf. Sci.* **2000**, *468*, 51–61.
- (55) Skorodumova, N. V.; Baudin, M.; Hermansson, K. Surface Properties of CeO₂ from First Principles. *Phys. Rev. B: Condens. Matter Mater. Phys.* **2004**, *69*, 075401.
- (56) Paier, J.; Penschke, C.; Sauer, J. Oxygen Defects and Surface Chemistry of Ceria: Quantum Chemical Studies Compared to Experiment. *Chem. Rev.* **2013**, *113*, 3949–3985.
- (57) Durban, M.; Bornscheuer, U. An Assay System for the Detection of Phospholipase C Activity. *Eur. J. Lipid Sci. Technol.* **2003**, *105*, 633–637.
- (58) Kurioka, S.; Matsuda, M. Phospholipase C Assay Using p-Nitrophenylphosphoryl-choline Together with Sorbitol and its Application to Studying the Metal and Detergent Requirement of the Enzyme. *Anal. Biochem.* **1976**, *75*, 281–289.
- (59) Zupan, J. R.; Cameron, T. A.; Anderson-Furgeson, J.; Zambryski, P. C. Dynamic FtsA and FtsZ localization and outer membrane alterations during polar growth and cell division in *Agrobacterium tumefaciens*. *Proc. Natl. Acad. Sci. U.S.A.* **2013**, *110*, 9060–9065.
- (60) Jelínková, A.; Malínská, K.; Simon, S.; Vehn, J. K.; Pařezová, M.; Pejchar, P.; Kubeš, M.; Martinec, J.; Friml, J.; Zažímalová, E.; Petrášek, J. Probing plant membranes with FM dyes: tracking, dragging or blocking? *Plant J.* **2010**, *61*, 883–892.
- (61) Monod, J. The growth of bacterial cultures. *Annu. Rev. Microbiol.* **1949**, *3*, 371–394.
- (62) Srinandan, C. S.; Elango, M.; Gnanadhas, D. P.; Chakravortty, D. Infiltration of Matrix-Non-producers Weakens the *Salmonella* Biofilm and Impairs Its Antimicrobial Tolerance and Pathogenicity. *Front. Microbiol.* **2015**, *6*, 1468.
- (63) Sehgal, A.; Lalatonne, Y.; Berret, J.-F.; Morvan, M. Precipitation–Redispersion of Cerium Oxide Nanoparticles with Poly(acrylic acid): Toward Stable Dispersions. *Langmuir* **2005**, *21*, 9359–9364.
- (64) Vernekar, A. A.; Das, T.; Ghosh, S.; Mughesh, G. A Remarkably Efficient MnFe₂O₄-based Oxidase Nanozyme. *Chem.—Asian J.* **2016**, *11*, 72–76.
- (65) Peterson, J. W. Bacterial Pathogenesis. In *Medical Microbiology*, 4th ed.; Baron, S., Ed.; University of Texas Medical Branch at Galveston: Galveston (TX), 1996.
- (66) Magill, S. S.; Edwards, J. R.; Bamberg, W.; Beldavs, Z. G.; Dumyati, G.; Kainer, M. A.; Lynfield, R.; Maloney, M.; McAllister-Hollod, L.; Nadle, J.; Ray, S. M.; Thompson, D. L.; Wilson, L. E.; Fridkin, S. K. Multistate Point Prevalence Survey of Health Care–Associated Infections. *N. Engl. J. Med.* **2014**, *370*, 1198–1208.
- (67) Saint, S.; Greene, M. T.; Krein, S. L.; Rogers, M. A. M.; Ratz, D.; Fowler, K. E.; Edson, B. S.; Watson, S. R.; Meyer-Lucas, B.; Masuga, M.; Faulkner, K.; Gould, C. V.; Battles, J.; Fakhri, M. G. A Program to Prevent Catheter Associated Urinary Tract Infection in Acute Care. *N. Engl. J. Med.* **2016**, *374*, 2111–2119.
- (68) Kardan-Yamchi, J.; Kazemian, H.; Battaglia, S.; Abtahi, H.; Foroushani, A. R.; Hamzelou, G.; Cirillo, D. M.; Ghodousi, A.; Feizabadi, M. M. Whole genome sequencing results associated with minimum inhibitory concentrations of 14 anti-Tuberculosis drugs among Rifampicin-resistant isolates of *Mycobacterium Tuberculosis* from Iran. *J. Clin. Med.* **2020**, *9*, 465.

(69) Kaniga, K.; Cirillo, D. M.; Hoffner, S.; Ismail, N. A.; Kaur, D.; Lounis, N.; Metchock, B.; Pfyffer, G. E.; Venter, A. A multilaboratory, multicountry study to determine Bedaquiline MIC quality control ranges for phenotypic drug susceptibility testing. *J. Clin. Microbiol.* **2016**, *54*, 2956–2962.

(70) Pinna, A.; Malfatti, L.; Galleri, G.; Manetti, R.; Cossu, S.; Rocchitta, G.; Migheli, R.; Serra, P. A.; Innocenzi, P. Ceria Nanoparticles for The Treatment of Parkinson-like Diseases Induced by Chronic Manganese Intoxication. *RSC Adv.* **2015**, *5*, 20432–20439.